Dynamical coupled-channels analysis of ^{1}H$(e,e'\pi)N$ reactions

B. Juliá-Díaz,[1,2] H. Kamano,[1] T.-S. H. Lee,[1,3] A. Matsuyama,[1,4] T. Sato,[1,5] and N. Suzuki[1,5]

[1]*Excited Baryon Analysis Center (EBAC), Thomas Jefferson National Accelerator Facility, Newport News, Virginia 23606, USA*

[2]*Department d'Estructura i Constituents de la Matèria and Institut de Ciències del Cosmos, Universitat de Barcelona, E-08028 Barcelona, Spain*

[3]*Physics Division, Argonne National Laboratory, Argonne, Illinois 60439, USA*

[4]*Department of Physics, Shizuoka University, Shizuoka 422-8529, Japan*

[5]*Department of Physics, Osaka University, Toyonaka, Osaka 560-0043, Japan*

(Received 13 April 2009; published 24 August 2009)

We have performed a dynamical coupled-channels analysis of available $p(e,e'\pi)N$ data in the region of $W \leqslant 1.6$ GeV and $Q^2 \leqslant 1.45$ (GeV/c)^2. The channels included are γ^*N, πN, ηN, and $\pi\pi N$ that has $\pi\Delta$, ρN, and σN components. With the hadronic parameters of the model determined in our previous investigations of $\pi N \to \pi N$, $\pi\pi N$ reactions, we have found that the available data in the considered $W \leqslant 1.6$ GeV region can be fitted well by only adjusting the bare $\gamma^*N \to N^*$ helicity amplitudes for the lowest N^* states in P_{33}, P_{11}, S_{11}, and D_{13} partial waves. The sensitivity of the resulting parameters to the amount of data included in the analysis is investigated. The importance of coupled-channels effect on the $p(e,e'\pi)N$ cross sections is demonstrated. The meson cloud effect, as required by the unitarity conditions, on the $\gamma^*N \to N^*$ form factors are also examined. Necessary future developments, both experimentally and theoretically, are discussed.

DOI: 10.1103/PhysRevC.80.025207 PACS number(s): 13.75.Gx, 13.60.Le, 14.20.Gk, 25.30.Rw

I. INTRODUCTION

The electromagnetic parameters characterizing the excited nucleons (N^*), in particular the $\gamma^*N \to N^*$ form factors, are important information for understanding the hadron structure within quantum chromodynamics (QCD). With the efforts in recent years, as reviewed in Ref. [1], the world data of $\gamma^*N \to \Delta(1232)$ form factors are now considered along with the electromagnetic nucleon form factors as the benchmark data for developing hadron structure models and testing predictions from lattice QCD calculations (LQCD). The main objective of this work is to explore the extent to which the available $p(e,e'\pi)N$ data in $W \leqslant 1.6$ GeV can be used to extract the $\gamma^*N \to N^*$ form factors for the N^* states up to the so-called second resonance region.

We employed a dynamical coupled-channels model developed in Refs. [2–6]. This work is an extension of our analysis [4] of pion photoproduction reactions. We therefore will only recall equations that are relevant to the coupled-channels calculations of $p(e,e'\pi)N$ cross sections. In the helicity-LSJ mixed-representation where the initial γN state is specified by its helicities λ_γ and λ_N and the final MB states by the $(LS)J$ angular-momentum variables, the reaction amplitude of $\gamma^*(\vec{q}, Q^2) + N(-\vec{q}) \to \pi(\vec{k}) + N(-\vec{k})$ at invariant mass W and momentum transfer $Q^2 = -q^\mu q_\mu = \vec{q}^{\,2} - \omega^2$ can be written within a Hamiltonian formulation [2] as (suppress the isospin quantum numbers)

$$T^J_{LS_N\pi N,\lambda_\gamma\lambda_N}(k,q,W,Q^2) = t^J_{LS_N\pi N,\lambda_\gamma\lambda_N}(k,q,W,Q^2) + t^{R,J}_{LS_N\pi N,\lambda_\gamma\lambda_N}(k,q,W,Q^2), \tag{1}$$

where $S_N = 1/2$ is the nucleon spin, $W = \omega + E_N(q)$ is the invariant mass of the γ^*N system, and the nonresonant amplitude is

$$\begin{aligned} t^J_{LS_N\pi N,\lambda_\gamma\lambda_N}(k,q,W,Q^2) &= v^J_{LS_N\pi N,\lambda_\gamma\lambda_N}(k,q,Q^2) \\ &+ \sum_{M'B'}\sum_{L'S'}\int k'^2dk' t^J_{LS_N\pi N,L'S'M'B'}(k,k',W) \\ &\times G_{M'B'}(k',W) v^J_{L'S'M'B',\lambda_\gamma\lambda_N}(k',q,Q^2). \end{aligned} \tag{2}$$

In the above equation, $G_{M'B'}(k',W)$ are the meson-baryon propagators for the channels $M'B' = \pi N, \eta N, \pi\Delta, \rho N, \sigma N$. The matrix elements $v^J_{LSMB,\lambda_\gamma\lambda_N}(k,q,Q^2)$, which describe the $\gamma N \to MB$ transitions, are calculated from tree diagrams of a set of phenomenological Lagrangians describing the interactions among $\gamma, \pi, \eta, \rho, \omega, \sigma, N$, and $\Delta(1232)$ fields. The details are given explicitly in Appendix F of Ref. [2]. The hadronic nonresonant amplitudes $t^J_{LS_N\pi N,L'S'M'B'}(k,k',W)$ are generated from the model constructed from analyzing the data of $\pi N \to \pi N$, $\pi\pi N$ reactions [3,6].

The resonant amplitude in Eq. (1) is

$$t^{R,J}_{LS_N\pi N,\lambda_\gamma\lambda_N}(k,q,W,Q^2) = \sum_{N^*_i,N^*_j}\left[\bar{\Gamma}^J_{N^*_i,LS_N\pi N}(k,W)\right]^* \times D_{i,j}(W)\bar{\Gamma}^J_{N^*_j,\lambda_\gamma\lambda_N}(q,W,Q^2), \tag{3}$$

where the dressed $N^* \to \pi N$ vertex $\bar{\Gamma}^J_{N^*_i,LS_N\pi N}(k,W)$ and N^* propagator $D_{i,j}(W)$ have been determined and given explicitly in Ref. [4]. The quantity relevant to our later discussions is the

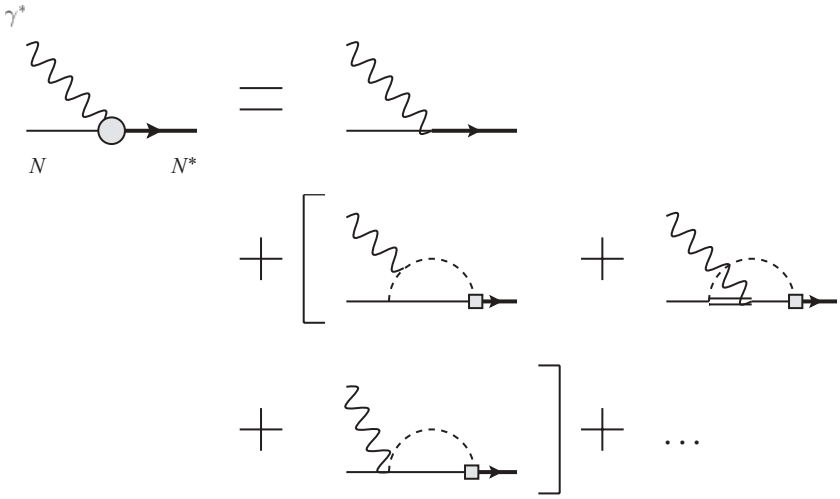

FIG. 1. Graphical illustration of the contribution to the πN intermediate state to the dressed $\gamma^* N \to N^*$ vertex defined by Eq. (4).

dressed $\gamma^* N \to N^*$ vertex function defined by

$$\bar{\Gamma}^J_{N^*,\lambda_\gamma\lambda_N}(q, W, Q^2) = \Gamma^J_{N^*,\lambda_\gamma\lambda_N}(q, Q^2) + \sum_{M'B'}\sum_{L'S'}\int k'^2 dk' \bar{\Gamma}^J_{N^*,L'S'M'B'}(k', W) \times G_{M'B'}(k', W) v^J_{L'S'M'B',\lambda_\gamma\lambda_N}(k', q, Q^2). \quad (4)$$

The second term of Eq. (4) is due to the mechanism where the nonresonant electromagnetic meson production takes place before the dressed N^* states are formed. This is illustrated in Fig. 1 for the contribution due to the $M'B' = \pi N$ intermediate state. Similar to what was defined in Ref. [7,8], we call this contribution the *meson cloud effect* to define precisely what will be presented in this article. We emphasize here that the meson cloud term in Eq. (4) is the necessary consequence of the unitarity conditions. How this term and the assumed bare N^* states are interpreted is obviously model dependent. This issue as well as the questions concerning the extractions of form factors at resonance pole positions will be discussed elsewhere and will not be addressed here.

Within the one-photon exchange approximation, the differential cross sections of pion electroproduction can be written as

$$\frac{d\sigma^5}{dE_{e'}d\Omega_{e'}d\Omega^*_\pi} = \Gamma_\gamma[\sigma_T + \epsilon\sigma_L + \sqrt{2\epsilon(1+\epsilon)}\sigma_{LT}\cos\phi^*_\pi + \epsilon\sigma_{TT}\cos 2\phi^*_\pi + h_e\sqrt{2\epsilon(1-\epsilon)}\sigma_{LT'}\sin\phi^*_\pi]. \quad (5)$$

Here $\Gamma_\gamma = [\alpha/(2\pi^2 Q^2)](E_{e'}/E_e)[|\vec{q}_L|/(1-\epsilon)]$; ϵ is defined by the electron scattering angle θ_e and the photon three-momentum $\vec{q}_L$ in the laboratory frame as $\epsilon = [1 + 2(|\vec{q}_L|^2/Q^2)\tan^2(\theta_e/2)]^{-1}$; h_e is the helicity of the incoming electron; ϕ^*_π is the angle between the π-N plane and the plane of the incoming and outgoing electrons. The quantities associated with the electrons are defined in the laboratory frame. However, structure functions of $\gamma^* N \to \pi N$ process, $\sigma_\alpha = \sigma_\alpha(W, Q^2, \cos\theta^*_\pi)$ ($\alpha = T, L, LT, TT, LT'$), are defined in the final πN center-of-mass system. The formula for calculating σ_α from the amplitudes defined by Eqs. (1)–(3) are given in Ref. [9].

In this first-stage investigation, we consider only the data of structure functions σ_α of $p(e,e'\pi^0)p$ [10,11] and $p(e,e'\pi^+)n$ [12,13] up to $W = 1.6$ GeV and $Q^2 = 1.45$ (GeV/c)^2. The availability of the data in the corresponding (W, Q^2) region is found in Table I. The resulting parameters are then confirmed against the original fivefold differential cross-section data [14].

TABLE I. Available structure function data at $Q^2 \leqslant 1.45$ (GeV/c)^2.

Q^2 (GeV/c)^2	$\gamma^* p \to \pi^0 p$	$\gamma^* p \to \pi^+ n$
0.3	–	$\sigma_T + \epsilon\sigma_L, \sigma_{LT}, \sigma_{TT}$ [12]
0.4	$\sigma_T + \epsilon\sigma_L, \sigma_{LT}, \sigma_{TT}$ [10]; $\sigma_{LT'}$ [11]	$\sigma_T + \epsilon\sigma_L, \sigma_{LT}, \sigma_{TT}$ [12]; $\sigma_{LT'}$ [13]
0.5	–	$\sigma_T + \epsilon\sigma_L, \sigma_{LT}, \sigma_{TT}$ [12][a]
0.525	$\sigma_T + \epsilon\sigma_L, \sigma_{LT}, \sigma_{TT}$ [10]	–
0.6	–	$\sigma_T + \epsilon\sigma_L, \sigma_{LT}, \sigma_{TT}$ [12][b]
0.65	$\sigma_T + \epsilon\sigma_L, \sigma_{LT}, \sigma_{TT}$ [10]; $\sigma_{LT'}$ [11]	$\sigma_{LT'}$ [13]
0.75	$\sigma_T + \epsilon\sigma_L, \sigma_{LT}, \sigma_{TT}$ [10]	–
0.9	$\sigma_T + \epsilon\sigma_L, \sigma_{LT}, \sigma_{TT}$ [10]	–
1.15	$\sigma_T + \epsilon\sigma_L, \sigma_{LT}, \sigma_{TT}$ [10]	–
1.45	$\sigma_T + \epsilon\sigma_L, \sigma_{LT}, \sigma_{TT}$ [10]	–

[a]The data are available up to $W = 1.51$ GeV.
[b]The data are available up to $W = 1.41$ GeV.

This procedure could overestimate/underestimate the errors of our analysis but is sufficient for the present exploratory investigation.

In Sec. II, we present the results from our analysis. Discussions on future developments are given in Sec. III.

II. ANALYSIS AND RESULTS

To proceed, we need to define the bare $\gamma^* N \to N^*$ vertex functions $\Gamma^J_{N^*,\lambda_\gamma\lambda_N}(q,Q^2)$ of Eq. (4). We parametrize these functions as

$$\Gamma^J_{N^*,\lambda_\gamma\lambda_N}(q,Q^2) = \frac{1}{(2\pi)^{3/2}}\sqrt{\frac{m_N}{E_N(q)}}\sqrt{\frac{q_R}{|q_0|}}G_\lambda(N^*,Q^2)\delta_{\lambda,(\lambda_\gamma-\lambda_N)}, \quad (6)$$

where q_R and q_0 are defined by $M_{N^*} = q_R + E_N(q_R)$ with N^* mass and $W = q_0 + E_N(q_0)$, respectively, and

$$G_\lambda(N^*,Q^2) = A_\lambda(N^*,Q^2), \quad \text{for transverse photon,} \quad (7)$$
$$= S_\lambda(N^*,Q^2), \quad \text{for longitudinal photon.} \quad (8)$$

For later discussions, we also cast the helicity amplitudes of the dressed vertex Eq. (4) into the form of Eq. (6) with dressed helicity amplitudes

$$\bar{A}_\lambda(N^*,Q^2) = A_\lambda(N^*,Q^2) + A^{\text{m.c.}}_\lambda(N^*,Q^2), \quad (9)$$
$$\bar{S}_\lambda(N^*,Q^2) = S_\lambda(N^*,Q^2) + S^{\text{m.c.}}_\lambda(N^*,Q^2), \quad (10)$$

where $A^{\text{m.c.}}_\lambda(N^*,Q^2)$ and $S^{\text{m.c.}}_\lambda(N^*,Q^2)$ are due to the meson cloud effect defined by the second term of Eq. (4).

With the hadronic parameters of the employed dynamical coupled-channels model determined in analyzing the πN reaction data [3,6], the only freedom in analyzing the electromagnetic meson production reactions is the electromagnetic coupling parameters of the model. If the parameters listed in Ref. [2] are used to calculate the nonresonant interaction $v^J_{L'S'M'B',\lambda_\gamma\lambda_N}(k',q)$ in Eqs. (2) and (4), the only parameters to be determined from the data of pion electroproduction reactions are the bare helicity amplitudes defined by Eq. (6). Such a highly constrained analysis was performed in Ref. [4] for pion photoproduction. It was found that the available data of $\gamma p \to \pi^0 p, \pi^+ n$ can be fitted reasonably well up to invariant mass $W \leqslant 1.6$ GeV. In this work we extend this effort to analyze the pion electroproduction data in the same W region.

We first try to fix the bare helicity amplitudes by fitting to the data of $\sigma_T + \epsilon\sigma_L$, σ_{LT}, and σ_{TT} of $p(e,e'\pi^0)p$ in Ref. [10] that covers almost all (W,Q^2) region we are considering (see Table I). In a purely phenomenological approach, we first vary all of the helicity amplitudes of 16 bare N^* states, considered in analyzing the $\pi N \to \pi N, \pi\pi N$ data [3,6], in the fits to the data. It turns out that only the helicity amplitudes of the first N^* states in S_{11}, P_{11}, P_{33}, and D_{13} are relevant in the considered $W \leqslant 1.6$ GeV. Thus in this article only the bare helicity amplitudes associated with those four bare N^* states (total 10 parameters) are varied in the fit and other bare helicity amplitudes are set to zero. The numerical fit is performed at each Q^2 independently, using the MINUIT library.

The results of our fits are the solid curves in the top three rows of Figs. 2–4. Clearly our results from this fit agree with the data well. We obtain similar quality of fits to the data of

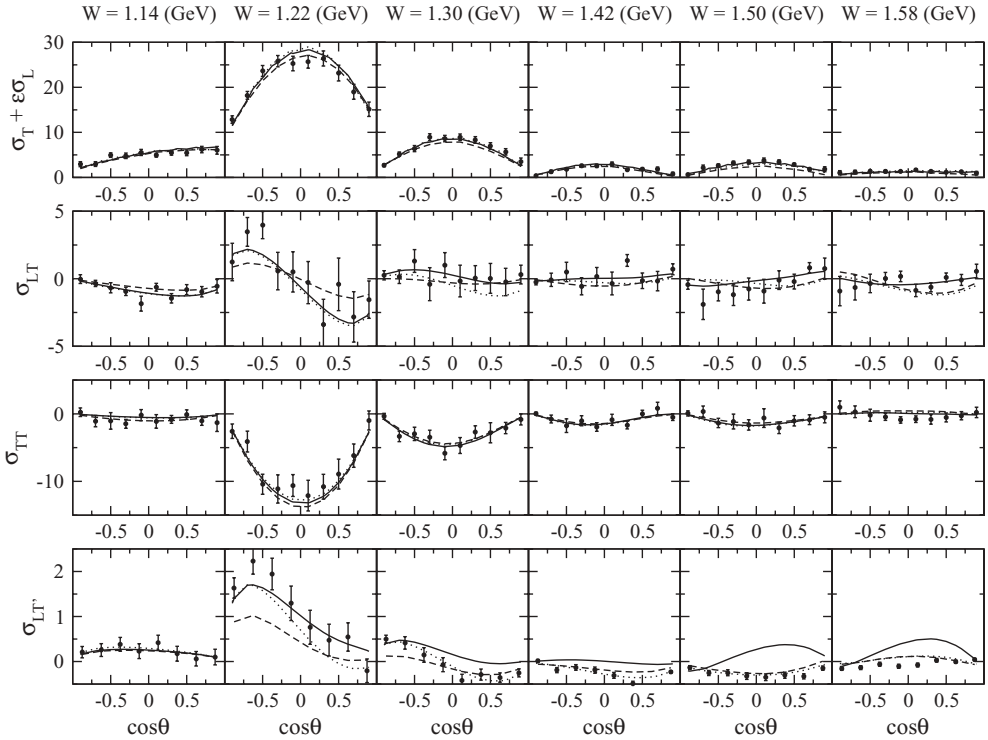

FIG. 2. Fit to $p(e,e'\pi^0)p$ structure functions at $Q^2 = 0.4$ (GeV/c)^2. Here $\theta \equiv \theta^*_\pi$. The solid curves are the results of Fit1, the dashed curves are of Fit2, and the dotted curves are of Fit3. (See text for the description of each fit.) The data are taken from Refs. [10,11].

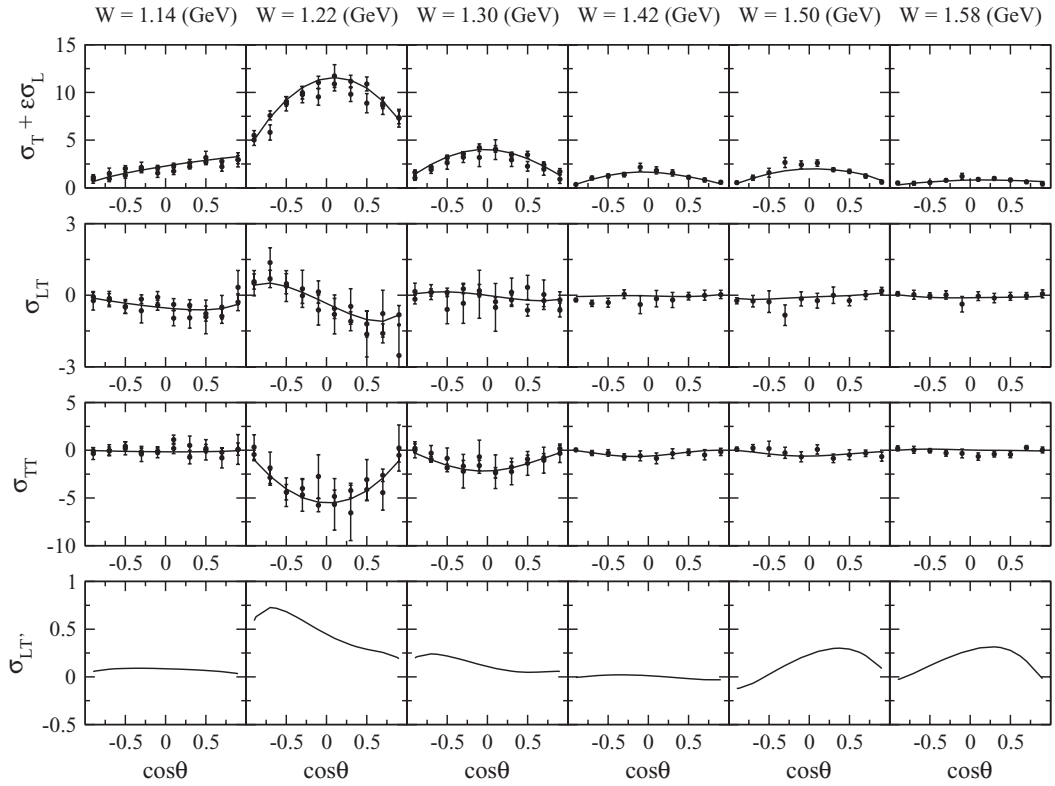

FIG. 3. Fit to $p(e,e'\pi^0)p$ structure functions at $Q^2 = 0.9$ (GeV/c)^2. Here $\theta \equiv \theta^*_\pi$. The data are taken from Ref. [10].

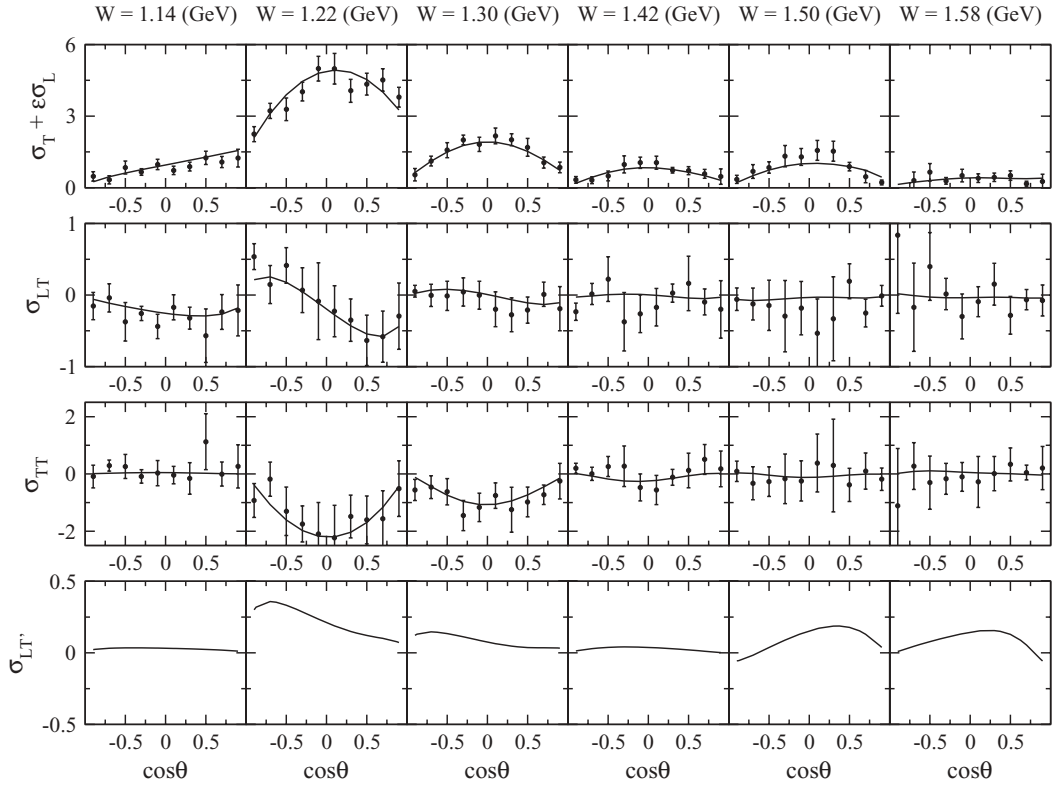

FIG. 4. Fit to $p(e,e'\pi^0)p$ structure functions at $Q^2 = 1.45$ (GeV/c)^2. Here $\theta \equiv \theta^*_\pi$. The data are taken from Ref. [10].

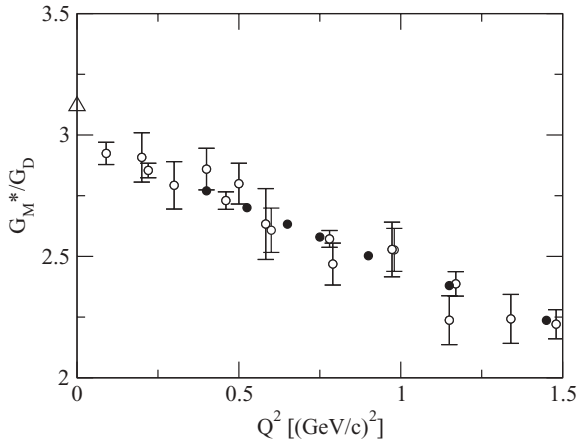

FIG. 5. G_M^* normalized by the dipole factor $G_D = [1 + Q^2/0.71\ (\mathrm{GeV}/c)^2]^{-2}$. The solid black circles at $Q^2 > 0$ are our fit to the values extracted from previous analyses (those values are taken from Ref. [4]). The triangle at $Q^2 = 0$ is from our photoproduction analysis [4].

Ref. [10] at other Q^2 values listed in Table I. We have also used the magnetic $M1$ form factor of $\gamma^* N \to \Delta(1232)$ extracted from previous analyses as data for fitting. The results are shown in Fig. 5. We refer the results of this fit to as "Fit1."

In Fig. 6, we present the G_M^*, G_E^*, and G_C^* form factors of $\gamma^* N \to \Delta(1232)$ transition obtained from Fit1 (solid points). In the same figure, we also show the meson cloud effect in the form factors. Within our model, it has a significant contribution at low Q^2 but rapidly decreases as Q^2 increases, particularly for G_E^* and G_C^*. These results are similar to the previous findings [7,15].

The helicity amplitudes of S_{11}, P_{11}, and D_{13} resulting from Fit1 are shown in Fig. 7. The solid circles are the absolute magnitude of the dressed helicity amplitudes (9) and (10). The errors there are assigned by MIGRAD in the MINUIT library. More detailed analysis of the errors is perhaps needed but will not be addressed here. The meson cloud effect (dashed curves), as defined by $A_\lambda^{\mathrm{m.c.}}$ and $S_\lambda^{\mathrm{m.c.}}$ of Eqs. (9) and (10) and calculated from the second term of Eq. (4), are the necessary consequence of the unitarity conditions. They do not include the bare helicity term determined here and are already fixed in the photoproduction analysis [4]. Within our model (and within Fit1), the meson cloud contribution is relatively small in S_{11} and $A_{1/2}$ of D_{13} even in the low Q^2 region.

Here we note that our helicity amplitudes defined in Eqs. (9) and (10) differ from the commonly used convention, say A_λ^{cnv} and S_λ^{cnv}, which is obtained from the imaginary part of the $\gamma^* N \to \pi N$ multipole amplitudes [16]. This definition leads to helicity amplitudes that are real, while our dressed amplitudes are complex. It was shown in Ref. [15] that for the $\Delta(1232)$ resonance our dressed helicity amplitudes (9) and (10) can be reduced to A_λ^{cnv} and S_λ^{cnv}, if we replace the Green function $G_{\pi N}$ with its principal value in all loop integrals appearing in the calculation. However, such reduction is not so trivial for higher resonance states because the unstable $\pi\Delta$, ρN, σN channels open, and thus the direct comparison of the helicity amplitudes from other analyses becomes unclear.

TABLE II. Ambiguity of resulting bare helicity amplitudes [the results are at $Q^2 = 0.4\ (\mathrm{GeV}/c)^2$]. The errors are assigned by MIGRAD in the MINUIT library.

	Fit1 (Ref. [10] data)	Fit2 (Refs. [10–13] data)	Fit3 (Refs. [10,11] data)
$S_{11}A_{1/2}$	100.80 ± 1.46	83.25 ± 1.21	48.29 ± 5.46
$S_{11}S_{1/2}$	-119.30 ± 20.41	-9.85 ± 1.69	-53.53 ± 4.75
$P_{11}A_{1/2}$	33.18 ± 2.11	-15.68 ± 1.00	20.17 ± 10.37
$P_{11}S_{1/2}$	37.29 ± 2.26	52.23 ± 3.16	131.00 ± 5.87
$P_{33}A_{3/2}$	-146.00 ± 0.60	-137.50 ± 0.56	-150.80 ± 1.03
$P_{33}A_{1/2}$	-54.47 ± 0.61	-62.57 ± 0.69	-46.29 ± 1.73
$P_{33}S_{1/2}$	7.85 ± 1.25	-7.66 ± 1.22	7.34 ± 1.69
$D_{13}A_{3/2}$	-44.01 ± 1.31	-67.01 ± 1.99	-98.63 ± 2.92
$D_{13}A_{1/2}$	97.11 ± 8.51	14.34 ± 1.26	70.02 ± 4.83
$D_{13}S_{1/2}$	-18.35 ± 1.37	19.43 ± 1.45	4.11 ± 2.76

At $Q^2 = 0.4\ (\mathrm{GeV}/c)^2$, the data of all structure functions both for $p(e,e'\pi^0)p$ and $p(e,e'\pi^+)n$ are available as seen in Table I. To see the sensitivity of the resulting helicity amplitudes to the amount of the data included in the fits, we further carry out two fits at this Q^2, referred to as Fit2 and Fit3, respectively. Fit2 (Fit3) further includes the data of Refs. [11–13] (Ref. [11]) in the fit in addition to those of Ref. [10] that are used in Fit1. This means that Fit2 includes all available data both from $p(e,e'\pi^0)p$ and $p(e,e'\pi^+)n$, whereas Fit3 includes the same data but from $p(e,e'\pi^0)p$ only. The results of each fit are the dashed and dotted curves in Fig. 2 for $p(e,e'\pi^0)p$ and Fig. 8 for $p(e,e'\pi^+)n$, respectively.

The resulting bare helicity amplitudes are listed in the third (Fit2) and fourth (Fit3) columns of Table II and compare with that from Fit1. The corresponding change in the $\gamma N \to \Delta(1232)$ form factors and the dressed helicity amplitudes are also shown as open circles and triangles in Figs. 6 and 7. A significant change among the three different fits is observed

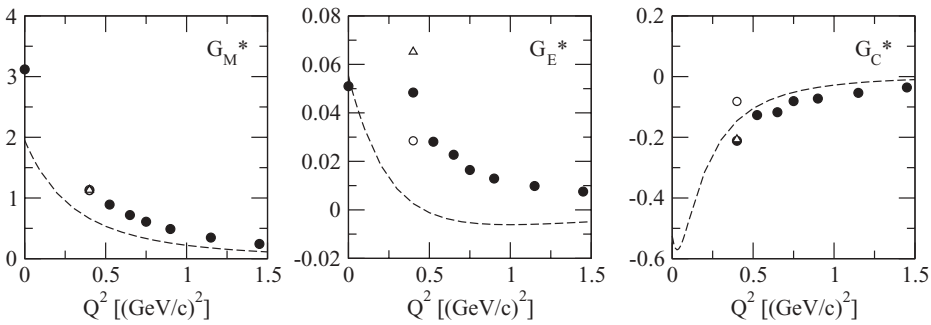

FIG. 6. The $\gamma^* N \to \Delta(1232)$ form factors. Solid points are from Fit1; dashed curves are the meson cloud contribution. Open circles and triangles at $Q^2 = 0.4\ (\mathrm{GeV}/c)^2$ are from Fit2 and Fit3, respectively. The three points are almost overlapped in G_M^*. The solid point at $Q^2 = 0$ is obtained from the photoproduction reaction analysis in Ref. [4].

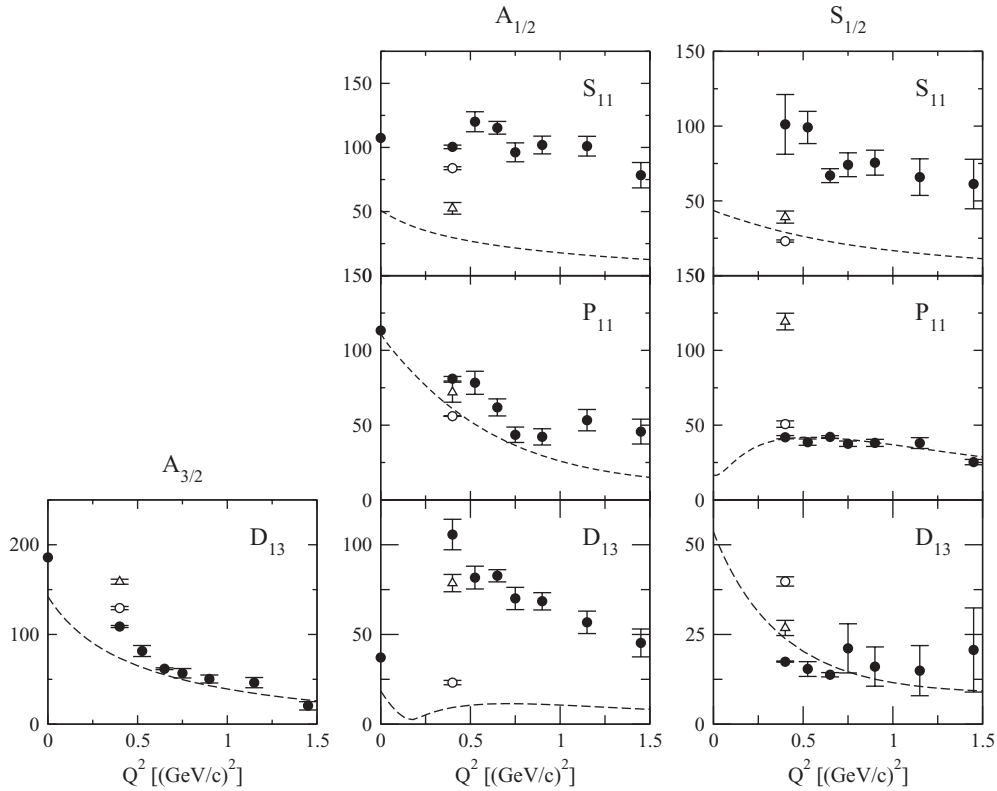

FIG. 7. Extracted helicity amplitudes for S_{11} at $W = 1535$ MeV (upper panels), P_{11} at $W = 1440$ MeV (middle panels), and D_{13} at $W = 1520$ MeV (lower panels). The meaning of each point and curve is the same as in Fig. 6.

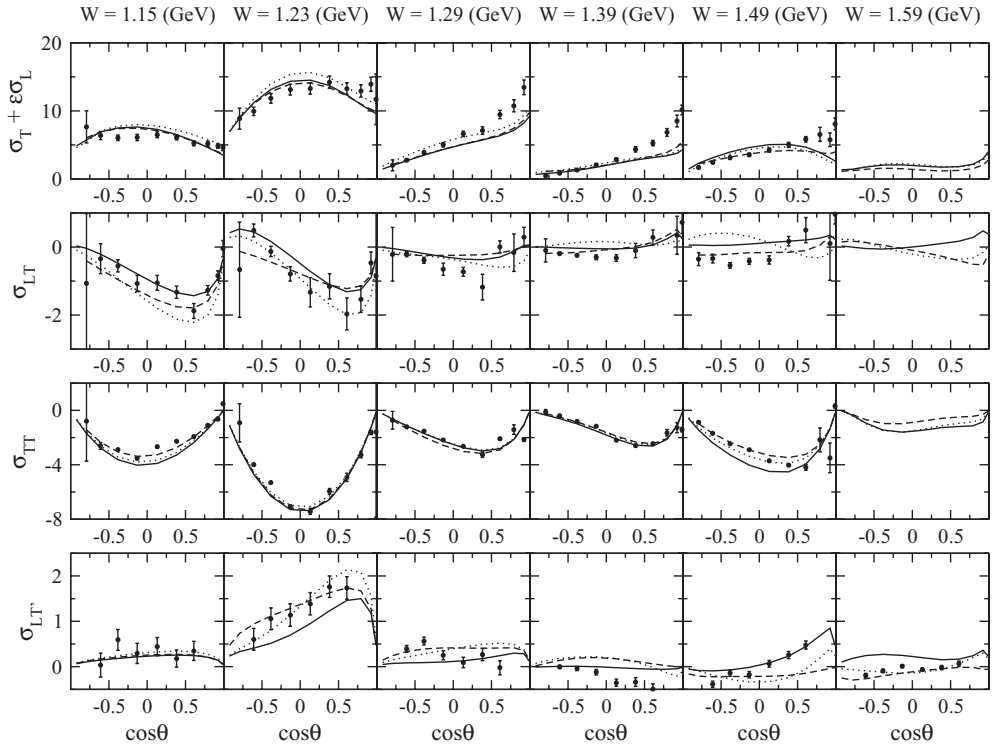

FIG. 8. Structure functions of $p(e,e'\pi^+)n$ at $Q^2 = 0.4$ (GeV/c)^2. Here $\theta \equiv \theta^*_\pi$. The solid curves are the results of Fit1, the dashed curves are of Fit2, and the dotted curves are of Fit3. (See text for the description of each fit.) As for the $\sigma_{LT'}$, results at $W = 1.14$, 1.22, 1.3, 1.38, 1.5, 1.58 GeV (from left to right of the bottom row) are shown, in which the data are available. The data in the figure are taken from Refs. [12,13].

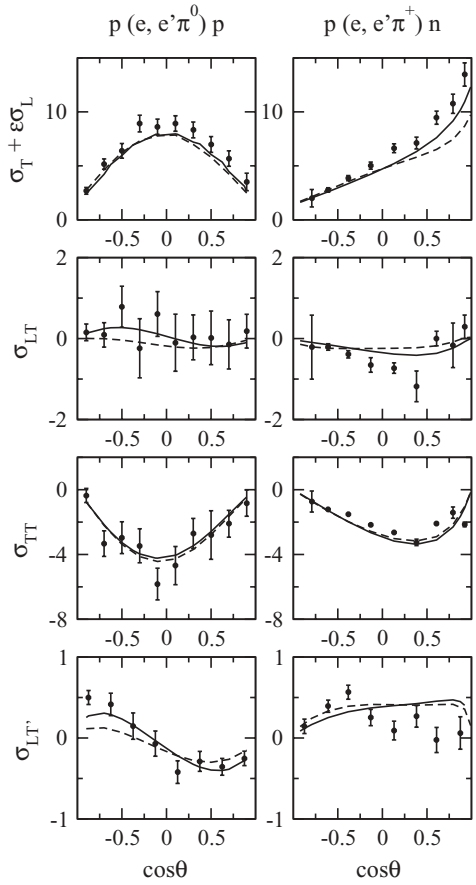

FIG. 9. Contribution of the S_{31} and P_{13} helicity amplitudes at $Q^2 = 0.4$ (GeV/c)^2. The left (right) panels are the structure functions of $p(e,e'\pi^0)p$ [$p(e,e'\pi^+)n$] reaction at $W = 1.3$ GeV ($W = 1.29$ GeV). Solid (dashed) curves are the results with (without) nonzero S_{31} and P_{13} bare helicity amplitudes. The parameters of Fit2 are used for the S_{11}, P_{11}, P_{33}, and D_{13} helicity amplitudes in both curves. The data are from Refs. [10–13].

in most of the results except G_M^* in P_{33}. This indicates that fitting the data listed in Table I is far from sufficient to pin down the $\gamma^*N \to N^*$ transition form factors up to $Q^2 = 1.45$ (GeV/c)^2. It clearly indicates the importance of obtaining data from complete or overcomplete measurements of most, if not all, of the independent $p(e,e'\pi)N$ polarization observables. Such measurements were made by Kelly *et al.* [17] in the $\Delta(1232)$ region and will be performed at JLab for wide ranges of W and Q^2 in the next few years [1].

It has been seen in Fig. 8 that all of our current fits underestimate σ_T of $p(e,e'\pi^+)n$ at forward angles. We find that this can be improved by further varying the S_{31} and P_{13} bare helicity amplitudes within their reasonable range. In Fig. 9, the results with the nonzero S_{31} and P_{13} bare helicity amplitudes (solid curves) are compared with the results without varying those amplitudes (dashed curves). The resulting values of the bare helicity amplitudes are $(A_{1/2}^{S_{31}}, S_{1/2}^{S_{31}}) = (121.6, 59.6)$ and $(A_{3/2}^{P_{13}}, A_{1/2}^{P_{13}}, S_{1/2}^{P_{13}}) = (-73.2, -42.9, 41.5)$. The parameters of Fit2 are used for S_{11}, P_{11}, P_{33}, and D_{13} in both curves. In the figure we have just shown the results at $W \sim 1.3$ GeV. We confirm that the same consequence is obtained also at other W and find that the P_{13} (S_{31}) has contributions mainly at low (high) W. We also find that the inclusion of the bare S_{31} and P_{13} helicity amplitudes does not change other structure functions than σ_T of $p(e,e'\pi^+)n$ (at most, most of the change is within the error). This indicates that those two helicity amplitudes are rather relevant to $p(e,e'\pi^+)n$ but not to $p(e,e'\pi^0)p$. As shown in Table I, however, not enough data are currently available for $p(e,e'\pi^+)n$ above $Q^2 = 0.4$ (GeV/c)^2. The data both of the $p(e,e'\pi^0)p$ and $p(e,e'\pi^+)n$ at same Q^2 values are desirable to pin down the Q^2 dependence of the S_{31} and P_{13} helicity amplitudes.

We now turn to show the coupled-channels effect. In Fig. 10, we see that when only the πN intermediate state is kept in the $M'B'$ summation of the nonresonant amplitude [Eq. (2)] and the dressed $\gamma^*N \to N^*$ vertices [Eq. (4)], the predicted total transverse and longitudinal cross sections σ_T and σ_L of $p(e,e'\pi^0)p$ are changed from the solid to dashed curves. This corresponds to examining the coupled-channels effect only on the electromagnetic (Q^2-dependent) part in the $\gamma^*N \to \pi N$ amplitude. All coupled-channels effects on the nonelectromagnetic interactions are kept in the calculations. We find that the coupled-channels effect tends to decrease when Q^2 increases. This is rather clearly seen in σ_T. In particular, the coupled-channels effect on σ_T at high $W \sim 1.5$ GeV is small (10–20%) already at $Q^2 = 0.4$ (GeV/c)^2. (The effect is about 30–40% at $Q^2 = 0$ [4].) This is understood as follows. In Eq. (3) we can further split the resonant amplitude t^R as $t^R = t^R_{\rm bare} + t^R_{\rm m.c.}$, where $t^R_{\rm bare}$ and $t^R_{\rm m.c.}$ are the same as t^R but replacing $\bar\Gamma^J_{N^*,\lambda_\gamma\lambda_N}$ with its bare part $\Gamma^J_{N^*,\lambda_\gamma\lambda_N}$ and meson cloud part [the second term of Eq. (4)], respectively. The coupled-channels effect shown in Fig. 10 comes from $t^J_{LS_N\pi N,\lambda_\gamma\lambda_N}$ and $t^R_{\rm m.c.}$. We have found that the relative importance of the coupled-channels effect in each part remains the same for increasing Q^2. However, the contribution of nonresonant mechanisms both on $t^J_{LS_N\pi N,\lambda_\gamma\lambda_N}$ and $t^R_{\rm m.c.}$ to the structure functions decreases for higher Q^2 compared with $t^R_{\rm bare}$. This explains the smaller coupled-channels effect compared with the photoproduction reactions [4]. The decreasing nonresonant interaction at higher Q^2 is due to its long range nature, thus indicating that higher Q^2 reactions provide a clearer probe of N^*. We obtain similar results also for $p(e,e'\pi^+)n$.

It is noted, however, that the above argument does not mean coupled-channels effect is negligible in the full $\gamma^*N \to \pi N$ reaction process. In the above analysis we kept the coupled-channels effect on the hadronic nonresonant amplitudes, the strong N^* vertices, and the N^* self-energy, which are Q^2 independent and remain important irrespective of Q^2. We have found in the previous analyses [3,6] that the coupled-channels effect on them is significant in all energy region up to $W = 2$ GeV.

In Fig. 11, we show the coupled-channels effect on the fivefold differential cross section defined by Eq. (5). The coupled-channels effects are significant at low W, whereas they are small at high W. This is consistent with the above discussions because the fivefold differential cross sections are dominated by σ_T. Here we also see that our full results (solid curves) are in good agreement with the original data, although

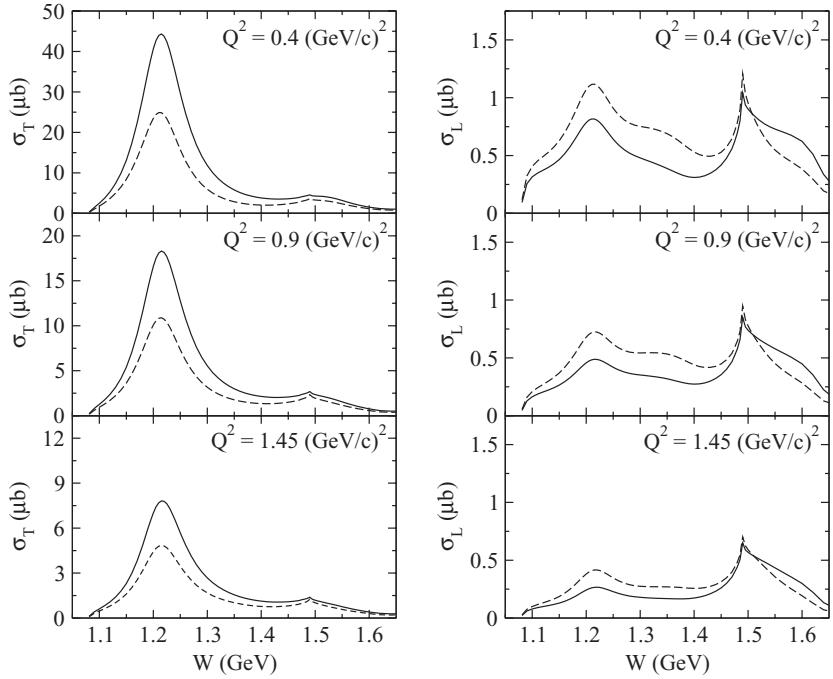

FIG. 10. Coupled-channels effect on the integrated structure functions $\sigma_T(W)$ and $\sigma_L(W)$ for $Q^2 = 0.4, 0.9, 1.45$ (GeV/c)^2 for $p(e,e'\pi^0)p$ reactions. The solid curves are the full results calculated with the bare helicity amplitudes of Fit1. The dashed curves are the same as solid curves but only the πN loop is taken in the $M'B'$ summation in Eqs. (2) and (4).

we performed the fits by using the structure function data listed in Table I.

III. SUMMARY AND OUTLOOK

In this work we have explored how the available $p(e, e'\pi)N$ data can be used to determine the $\gamma^*N \to N^*$ transition form factors within dynamical coupled-channels models [2–6]. Within the available data, the $\gamma^*N \to N^*$ bare helicity amplitudes of the first N^* states in S_{11}, P_{11}, P_{33}, and D_{13} can be determined in the considered energy region $W \leqslant 1.6$ GeV. We further observe that some of these parameters cannot be determined well. The uncertainties could be due to the limitation that data of only 4 of 11 independent $p(e,e'\pi)N$ observables are available for our analysis. Clearly, the data from the forthcoming measurements of double and triple polarization observables at JLab will be highly desirable to make progress.

Also, it was found that the underestimation of the σ_T of $p(e,e'\pi^+)n$ at forward angles can be improved by further considering the S_{31} and P_{13} bare helicity amplitudes. Furthermore, these amplitudes can have relevant contribution to $p(e,e'\pi^+)n$, but not to $p(e,e'\pi^0)p$. The $p(e,e'\pi^+)n$ data of wide Q^2 region

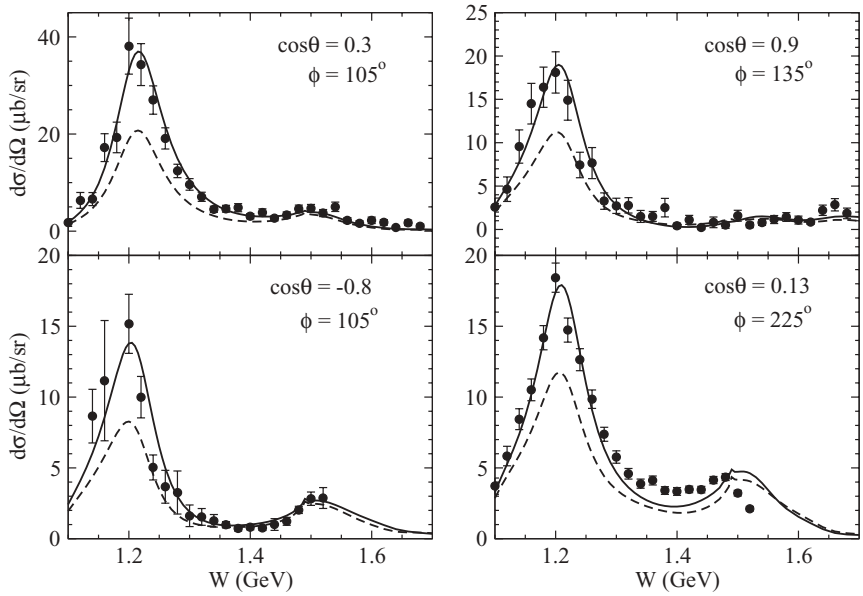

FIG. 11. Coupled-channels effect on the fivefold differential cross sections $\Gamma_\gamma^{-1}[d\sigma^5/(dE_{e'}d\Omega_{e'}d\Omega_\pi^*)]$ of $p(e,e'\pi^0)p$ (upper panels) and $p(e,e'\pi^+)n$ (lower panels) at $Q^2 = 0.4$ (GeV/c)^2. Here $\theta \equiv \theta_\pi^*$ and $\phi \equiv \phi_\pi^*$. The solid curves are the full results calculated with the bare helicity amplitudes of Fit1. The dashed curves are the same as the solid curves but only the πN loop is taken in the $M'B'$ summation in Eqs. (2) and (4). The data are taken from Ref. [14].

as well as $p(e,e'\pi^0)p$ seem necessary for determining the Q^2 dependence of the S_{31} and P_{13} helicity amplitudes.

For testing theoretical predictions from hadron structure calculations such as LQCD, the quantities of interest are the residues of the $\gamma^*N \to \pi N$ amplitudes, defined by Eqs. (1)–(4), at the corresponding resonance poles. If the resonance poles are associated with the amplitude $t^{R,J}_{LS_N\pi N,\lambda_\gamma\lambda_N}(k,q,W,Q^2)$ of Eq. (3), the extracted residues are directly related to the dressed form factors $\bar{\Gamma}^J_{N^*,L'S'M'B'}(k',W)$. An analytic continuation method for extracting these information has been developed [18], and our results along with other hadronic properties associated nucleon resonances will be published elsewhere. Here we only mention that the extracted form factors are complex and some investigations are needed to see how they can be compared with the helicity amplitudes, which are real numbers, listed by PDG [19]. In a Hamiltonian formulation as taken in our dynamical approach, the physical meanings of poles and residues are well defined in textbooks [20,21].

ACKNOWLEDGMENTS

We would like to thank Dr. K. Park for sending the structure function data from CLAS. This work is supported by the US Department of Energy, Office of Nuclear Physics Division, under Contract No. DE-AC02-06CH11357, and Contract No. DE-AC05-06OR23177, under which Jefferson Science Associates operates Jefferson Lab, by the Japan Society for the Promotion of Science, Grant-in-Aid for Scientific Research(C) 20540270, and by a CPAN Consolider INGENIO CSD 2007-0042 contract and Grant No. FIS2008-1661 (Spain). This work used resources of the National Energy Research Scientific Computing Center that is supported by the Office of Science of the US Department of Energy under Contract No. DE-AC02-05CH11231.

[1] V. Burkert and T.-S. H. Lee, Int. J. Mod. Phys. E **13**, 1035 (2004).
[2] A. Matsuyama, T. Sato, and T.-S. H. Lee, Phys. Rep. **439**, 193 (2007).
[3] B. Juliá-Díaz, T.-S. H. Lee, A. Matsuyama, and T. Sato, Phys. Rev. C **76**, 065201 (2007).
[4] B. Juliá-Díaz, T.-S. H. Lee, A. Matsuyama, T. Sato, and L. C. Smith, Phys. Rev. C **77**, 045205 (2008).
[5] J. Durand, B. Juliá-Díaz, T.-S. H. Lee, B. Saghai, and T. Sato, Phys. Rev. C **78**, 025204 (2008).
[6] H. Kamano, B. Juliá-Díaz, T.-S. H. Lee, A. Matsuyama, and T. Sato, Phys. Rev. C **79**, 025206 (2009).
[7] B. Juliá-Díaz, T.-S. H. Lee, T. Sato, and L. C. Smith, Phys. Rev. C **75**, 015205 (2007).
[8] T. Sato and T.-S. H. Lee, Phys. Rev. C **54**, 2660 (1996).
[9] T. Sato and T.-S. H. Lee, J. Phys. G **36**, 073001 (2009).
[10] K. Joo *et al.* (CLAS Collaboration), Phys. Rev. Lett. **88**, 122001 (2002).
[11] K. Joo *et al.* (CLAS Collaboration), Phys. Rev. C **68**, 032201 (2003).
[12] H. Egiyan *et al.* (CLAS Collaboration), Phys. Rev. C **73**, 025204 (2006).
[13] K. Joo *et al.* (CLAS Collaboration), Phys. Rev. C **72**, 058202 (2005).
[14] CLAS Physics Database, JLab (Hall B), http://clasweb.jlab.org/cgi-bin/clasdb/db.cgi.
[15] T. Sato and T.-S. H. Lee, Phys. Rev. C **63**, 055201 (2001).
[16] I. G. Aznauryan, V. D. Burkert, and T.-S. H. Lee, arXiv:0810.0997v2 [nucl-th].
[17] J. Kelly *et al.* (Jefferson Laboratory E91011 and Hall A Collaborations), Phys. Rev. Lett. **95**, 102001 (2005).
[18] N. Suzuki, T. Sato, and T.-S. H. Lee, Phys. Rev. C **79**, 025205 (2009).
[19] C. Amsler *et al.*, Phys. Lett. **B667**, 1 (2008).
[20] M. L. Goldberger and K. M. Watson, *Collision Theory* (Dover, Mineola, NY, 2004).
[21] H. Feshbach, *Theoretical Nuclear Physics: Nuclear Reactions* (John Wiley & Sons, New York, 1992).